



Original Research Paper

Structural and optoelectronic properties of alloyed $\text{Sn}_x\text{Mn}_{1-x}\text{S}$ thin filmsPo-Chia Huang^{a,b}, Muhammad Omar Shaikh^b, Sheng-Chang Wang^{b,*}^a Department of Materials Science and Engineering, National Cheng Kung University, Tainan 701, Taiwan^b Department of Mechanical Engineering, Southern Taiwan University of Science and Technology, Tainan 710, Taiwan

ARTICLE INFO

Article history:

Received 21 September 2015

Received in revised form 8 March 2016

Accepted 9 March 2016

Available online 16 March 2016

Keywords:

Tin sulfide

Metastable phase

Hot injection synthesis

Photo-electrochemical

ABSTRACT

This study finds that doping tin mono-sulfide (SnS) with different concentrations of manganese (Mn) (0–30wt%) results in a competition for anion bonding between tin and manganese during the hot-injection synthesis of the nanoparticles, creating lattice structures with strained crystallites and hence favoring the formation of the metastable zinc blende phase that has the crystal structure of sphalerite, a zinc ore. A typical hot-inject process was used to synthesize the SnS nanoparticles using oleic acid and oleylamine as solvents to produce the tin (doped with manganese) and sulfur precursors, respectively. We obtained a purely zinc blende phase at 260 °C when the doping concentration of Mn was increased to 30% while the stable orthorhombic phase was synthesized without doping. Powder X-ray diffraction (PXRD), High Resolution Transmission Electron Microscopy (HR-TEM) and Selected Area Electron Diffraction (SAED) results confirm the presence of the zinc blende phase at 30% Mn doping concentration. Ultraviolet–Vis–Near Infrared (UV–Vis–NIR) spectra show absorption onset at 980 nm for the orthorhombic phase and 840 nm for the zinc blende phase, and this blue shift can be attributed to the change in crystal phase structure. Electron spectroscopy for chemical analysis (ESCA) data shows that Mn^{2+} is doped substitutionally in place of Sn^{2+} , while the strong presence of Sn^{4+} is due to the low enthalpy during the formation of tin vacancies. Doped SnS thin films without any catalysts were spin-coated on fluorine doped tin oxide (FTO) substrates and used as a working electrode in a photo-electrochemical cell and show photocurrent densities up to $53.26 \mu\text{A}/\text{cm}^2$ at an applied potential of -1 V . These narrow band gap and low cost nanocrystals can be used for applications in future solar cells and other optoelectronic devices.

© 2016 The Society of Powder Technology Japan. Published by Elsevier B.V. and The Society of Powder Technology Japan. All rights reserved.

1. Introduction

The electronic, optical and photonic properties of semiconductor nanocrystals are strongly phase dependent, and recent research in synthesizing and characterizing the metastable zinc blende phase highlights this fact. SnS has the advantages of being naturally abundant, nontoxic, stable under ambient conditions, has a high p type conductivity [1] (hole mobility $\sim 90 \text{ cm}^2 \text{ V}^{-1} \text{ s}^{-1}$ [2]), a high absorption coefficient (10^4 – 10^5 cm^{-1} at the fundamental absorption edge which varies with the phase [3]), and a wide absorption range (band gap $\sim 1.3 \text{ eV}$ [4–8]) and thus theoretically possesses all the qualities for efficient absorption of solar energy and is suitable for incorporation into photovoltaic cells [9,10] and a variety of other optoelectronic devices [11].

An interest in the highly symmetrical zinc blende (ZB) phase arises from the fact that its structure and optical properties are

very different from the bulk and more stable orthorhombic (OR) phase. The local coordination of atoms in a crystal lattice plays an important role in influencing the physical and chemical properties of the material [7,9,12–15]. It has been observed that the metastable zinc blende phase appears first during crystallization from solution because its formation is kinetically faster, but eventually transforms into the thermodynamically more stable orthorhombic phase as more energy is provided by increasing the reaction time or temperature [14].

Tin sulfide nanostructures have been synthesized in various forms, including granular [5], nano branch structure [16], fullerene nanoparticles [17], layered nano-crystals [18,19], nanorods [20], nano-linear [21] and nanobelts [22] using various techniques, like hydrothermal, solvothermal, pyrolysis and microwave irradiation among others [4–6,8,18,23]. While in most of the research the final phase obtained is orthorhombic, less work has been reported on the controlled synthesis of the zinc blende phase. Deng et al. [7] synthesized zinc blende SnS nanoparticles of sizes 8, 60 and 700 nm using oleylamine as the solvent and Hexamethyldisilazane

* Corresponding author. Tel./fax: +886 2533131 3548.

E-mail address: scwang@stust.edu.tw (S.-C. Wang).

(HMDS) as the surfactant by varying the final temperature from 150 °C to 280 °C. The same group also published a report synthesizing 2–5 μm long single crystalline ultrathin SnS nanoribbons that grow via a metastable to stable phase transition and display dual phase intermediate heterostructures with zinc blende nanosphere heads and orthorhombic nanoribbon tails [15]. Greyson et al. [12] synthesized tetrahedral zinc blende SnS nano- and microcrystals by thermally decomposing tin chloride and elemental sulfur in oleylamine at mild temperatures (170 °C), but when the SnS tetrahedrons were heated to 250 °C in oleylamine for 3 h, a nearly complete transformation from zinc blende to orthorhombic phase was observed. Avellaneda et al. [13] synthesized polymorphic zinc blende and orthorhombic thin films of SnS by chemical deposition. Sinsermsuksakul et al. [24] recently studied the effects of antimony doping (1–5%) in the pulsed-CVD synthesis of SnS thin films in an effort to reduce the hole concentration and change the conduction type (p to n) for future utilization in the construction of SnS thin film solar cells with p-n homo junctions. Herein, we report the synthesis of SnS nanocrystals doped with different concentrations of Mn and utilize thin films of these materials as photoelectrodes for water splitting. To the best of our knowledge, no report has yet been published about the effects of doping Mn on the crystal phase and the optoelectronic properties of SnS.

2. Experimental

2.1. Materials

Tin(II) oxide (SnO, SHOWA, 99%), oleic acid (OA, $\text{C}_{18}\text{H}_{34}\text{O}_2$, Sigma Aldrich, 66–88%), manganese (II) oxide (MnO, Alfa Aesar, 99%), sulfur powder (S, Sigma Aldrich, 98%), oleylamine (OLA, $\text{C}_{18}\text{H}_{37}\text{N}$, ACROS, 90%), 1-octadecene (ODE, $\text{C}_{18}\text{H}_{36}$, ACROS, 90%), hexane (C_6H_{14} , Mallinckrodt, 90%), ethanol ($\text{H}_3\text{CH}_2\text{OH}$, OSAKA, 99%), and acetone (CH_3COCH_3 , OSAKA, 99.5%). All chemicals were used as received without further purification.

2.2. Synthesis

In this study we prepare SnS nanoparticles using thermal decomposition via a wet chemical synthesis route, as it complements the hot injection synthesis technique in which injection of precursors into a preheated solvent can induce rapid nucleation, and this is vital for obtaining nanoparticles with narrow size distributions [25]. In a typical synthesis experiment, 1.35 g of SnO was mixed with 13.5 ml OA and 3 ml of 1-ODE in a three-neck flask and heated to 110 °C under argon gas inflow and constant magnetic stirring, and held there for 15 min to remove all the excess water. The mixture was heated further up to 310 °C and held there for an hour to form the tin precursor ($\text{Sn}(\text{OA})_x$), after which it was cooled down to 130 °C. Simultaneously the sulfur precursor (S-OLA) was prepared by heating a mixture of 0.45 mmol of elemental sulfur powder and 9 ml OLA at 130 °C under magnetic stirring and argon gas inflow. Using glass syringes the hot sulfur precursor was quickly injected into the tin precursor and the final temperature was maintained at constant intervals between 130 °C and 310 °C for an hour before being cooled to room temperature. The resulting SnS nanoparticle solution was then added to ethanol and acetone in the ratio 1:9:9 and centrifuged at 5000 rpm for 15 min. This process was repeated three times to wash away all the organic solvents, and the final product was dried in a vacuum and redispersed in hexane. The doped SnS (Mn) nanoparticles were synthesized by adding different concentrations of manganese oxide (0–30 wt.%) during the synthesis of the tin precursor, resulting in a tin–manganese–oleate complex ($\text{Sn}_{1-x}\text{Mn}_x(\text{OA})_x$). All the

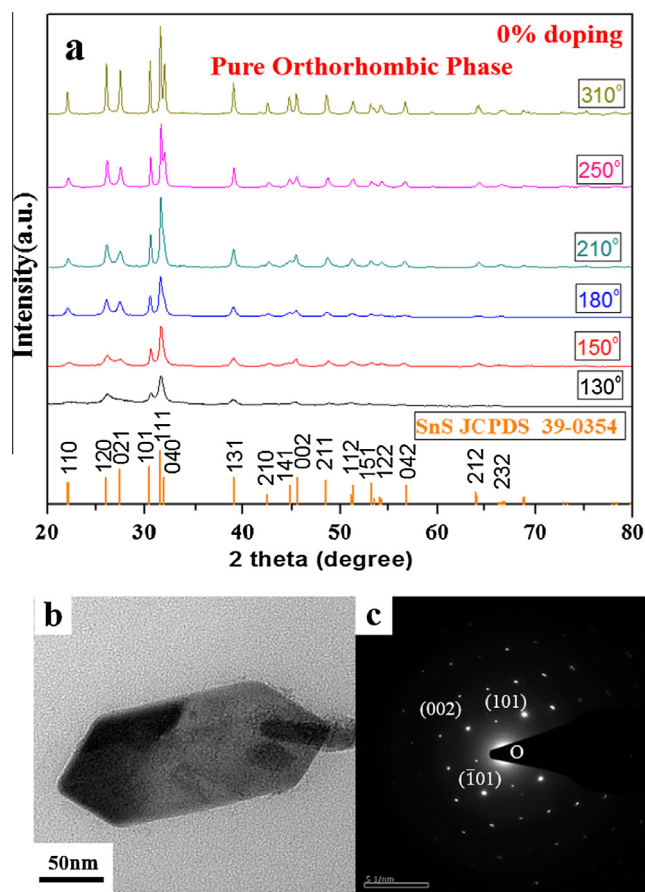


Fig. 1. (a) PXRD of SnS nanocrystals without Mn doping observed at different final reaction temperatures. (b) TEM image at the final reaction temperature of 310 °C showing an elongated hexagonal nanosheet where the horizontal axis corresponds to the (101) orthorhombic plane. (c) Orthorhombic phase of SnS as confirmed by the SAED pattern of single nanosheet.

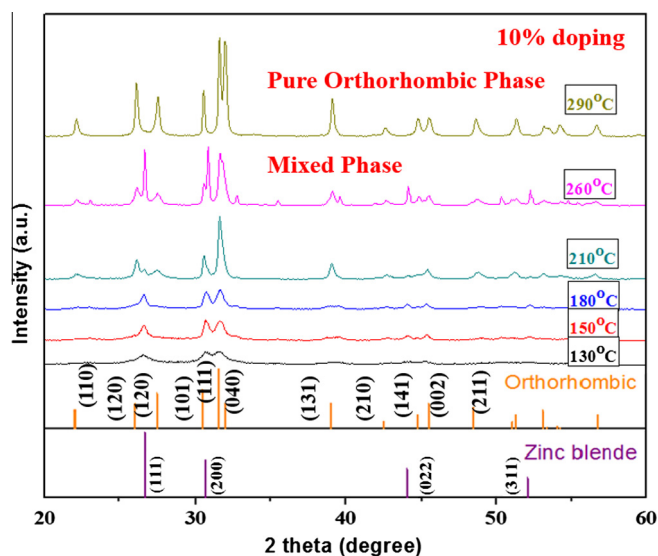


Fig. 2. PXRD pattern of SnS nanocrystals with 10 wt.% Mn doping obtained at different final reaction temperatures.

other steps remained the same. Thin films of doped and undoped SnS were prepared by spin coating a solution of the obtained nanocrystals (2 mg) in toluene (2 ml) on transparent FTO coated

glass substrates. The FTO/glass substrates were subjected to oxygen plasma for 30 s prior to the spin coating process to obtain improved binding of the SnS thin films to the FTO surface. Photo-electrochemical tests of obtained thin films were performed in a conventional three-electrode system with 0.1 M Na_2SO_4 electrolyte (pH = 7) using the SnS thin films as the working electrode, platinum gauze as the counter electrode and Ag/AgCl as the reference.

2.3. Characterizations

PXRD measurements were made on a D2 Phaser, BRUKER diffractometer with Cu $K\alpha$ radiation ($\lambda = 1.54060 \text{ \AA}$) at a scan rate of 0.025 s^{-1} to analyze the phase structure of the nanocrystals. HR-TEM was performed on a field emission gun transmission electron microscope (Tecnai G2 G20 FEG-TEM, Philips) operating at 200 kV. The dried powdered sample was dispersed in hexane to an appropriate concentration, and then drop coated on ultrathin carbon coated mesh copper grids and dried in the oven at $80 \text{ }^\circ\text{C}$ for an hour before being sent for TEM analysis. UV–Vis–NIR absorption spectra were recorded at room temperature on thin films of SnS spin coated on glass substrates and annealed at $80 \text{ }^\circ\text{C}$ (Laurell spin coater (Model no: WS-400BZ-6NPP)) using the JASCO V-670 spectrophotometer that is equipped with an integrating sphere. XPS experiments were performed on a PHI-5000C ESCA system (Perkin Elmer) using Mg $K\alpha$ radiation ($h\nu = 1253.6 \text{ eV}$). The photo-electrochemical properties were measured in ambient

conditions under irradiation of a 300 W Xe lamp ($\lambda > 420 \text{ nm}$, PLS-SXE300/300UV, Trusttech Co., Ltd. Beijing) having a power density of 50 mW cm^{-2} . The potential was swept from 0 to -1.0 V (vs. Ag/AgCl) at a sweep rate of 10 mV/s .

3. Results and discussion

The crystal structure of the undoped SnS nanocrystals synthesized at different final reaction temperatures was observed using PXRD. The crystalline phase for all reaction temperatures matches well with the stable orthorhombic phase ($a = 4.148 \text{ \AA}$, $b = 14.18 \text{ \AA}$, $c = 4.177 \text{ \AA}$, JCPDS 39-0354), and no other impurity phases were detected. At low temperatures the peaks are broad and not well formed, but at higher temperatures the peaks are sharper with higher intensities, thus showing high crystallinity and good grain growth (Fig. 1a). The TEM image at $310 \text{ }^\circ\text{C}$ (Fig. 1b) with an electron beam incident direction of (010) shows the formation of a thin elongated hexagonal single crystal SnS that has grown to about 230–250 nm along the orthorhombic (101) plane, while still maintaining the sheet like structure. At no temperature was the zinc blende phase identified.

SnS nanocrystals were then doped with 10 wt.% Mn and held at different final temperatures to analyze the phase changes induced by doping. Lower temperatures ($130\text{--}210 \text{ }^\circ\text{C}$) show peaks at 30.70° and 44.05° corresponding to the (111) and (022) planes of the zinc blende phase ($a = 5.41 \text{ \AA}$), respectively. However, the crystallinity

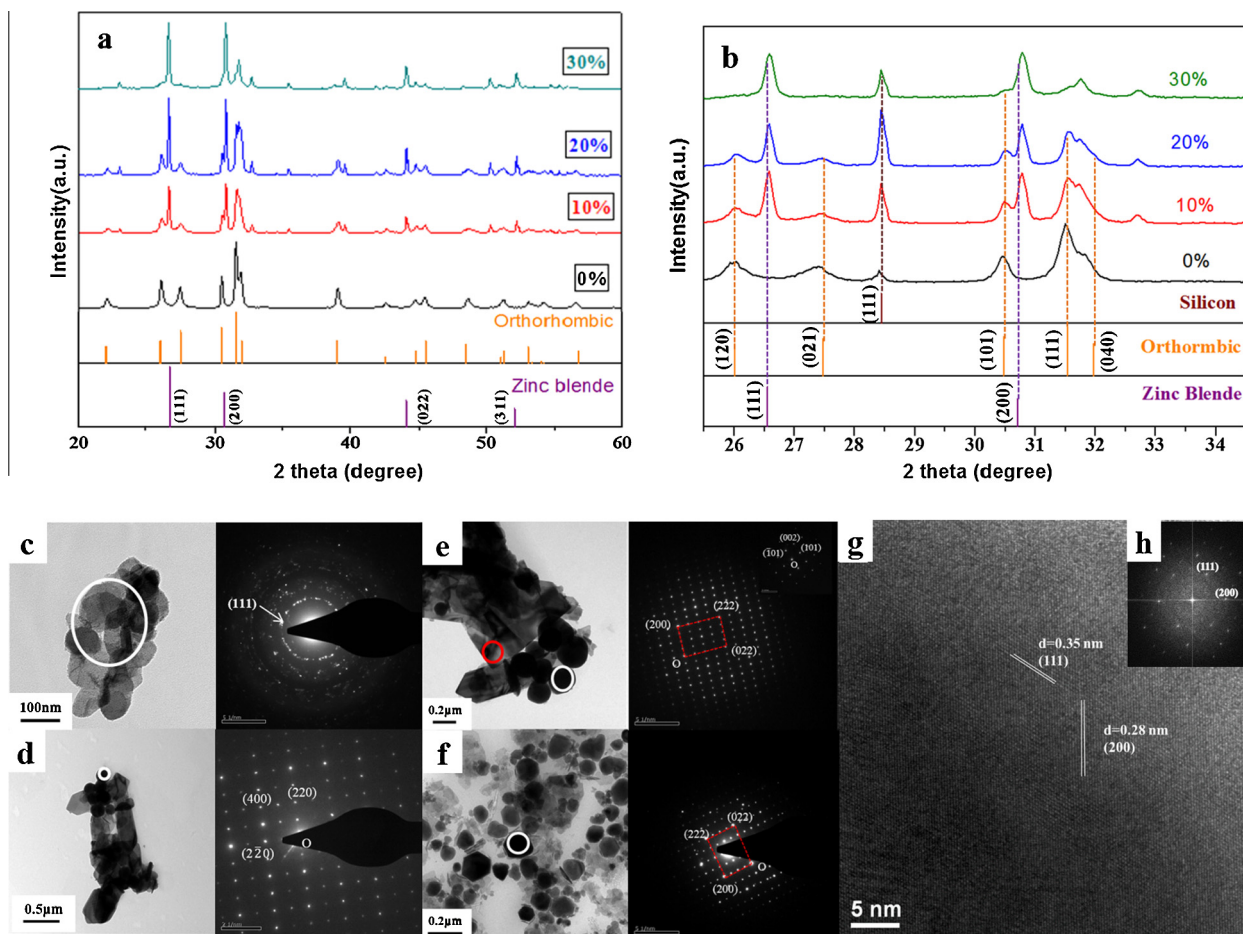


Fig. 3. (a) PXRD of SnS nanocrystals doped with Mn (0–30 wt.%) with the final reaction temperature maintained at $260 \text{ }^\circ\text{C}$ and (b) enlarged PXRD pattern from $25\text{--}35^\circ$ showing the pure zinc blende phase at 30 wt.% Mn doping. (c–f) TEM images and SAED patterns for SnS doped nanocrystals for 0, 10, 20 and 30 wt.% Mn respectively. (g) HRTEM image of near spherical zinc blende nanoparticles obtained at 30 wt.% Mn doping, and (h) the corresponding indexed fast Fourier transform (FFT) revealing single crystal structure along the (111) and (200) planes of zinc blende.

of the zinc blende phase obtained at these lower temperatures is relatively poor, as shown by the presence of broad peaks (Fig. 2). As the temperature is increased (210–260 °C), sharp peaks begin

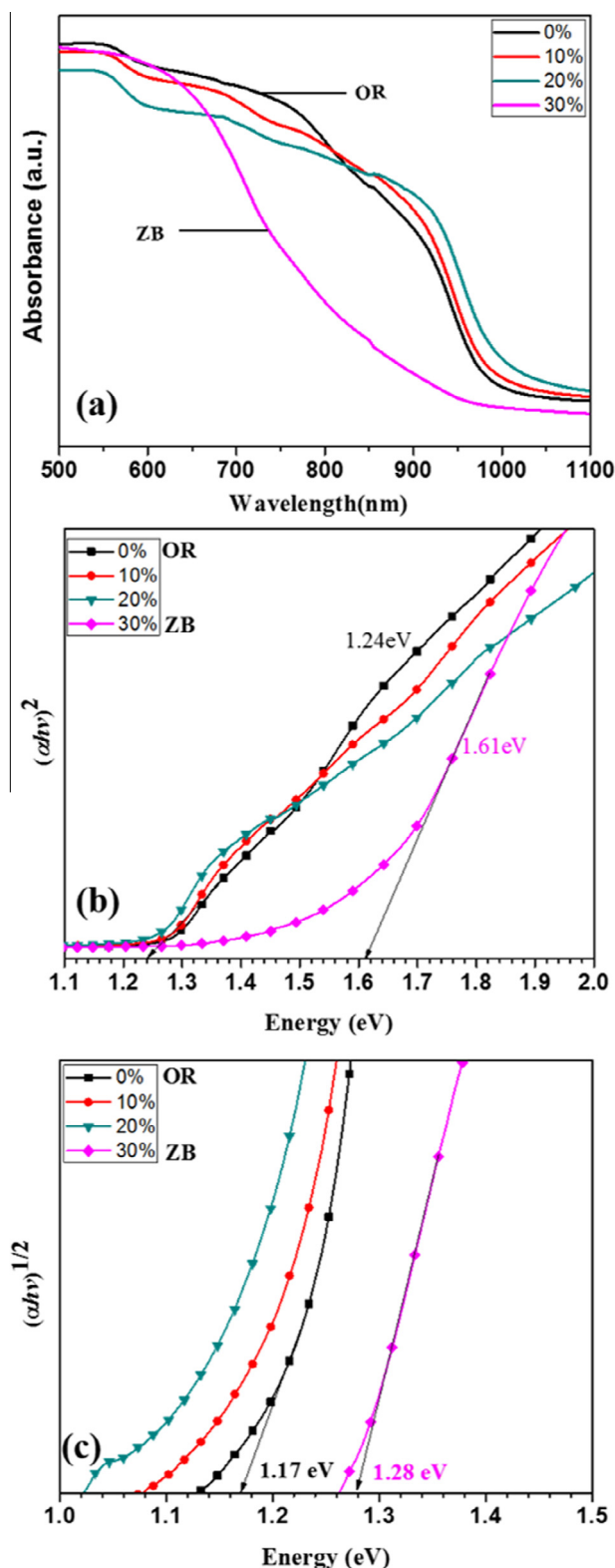


Fig. 4. (a) Plot of UV–Vis–NIR absorption spectrum of various concentrations of Mn doped SnS nanocrystals spin coated on glass substrates, (b) plot of $(\alpha h\nu)^2$ versus $h\nu$ (eV) showing direct band gap, and (c) plot of $(\alpha h\nu)^{1/2}$ versus $h\nu$ (eV) showing the indirect band gap of Mn doped SnS (0–30 wt.%) thin film.

to form that correspond to the (101) and (111) planes of orthorhombic SnS, while still retaining the (111) and (022) planes of zinc blende, resulting in a mixed phase structure. As the temperature is increased to 290 °C, all of the peaks corresponding to the zinc blende phase disappear, resulting in a pure orthorhombic phase. The presence of the zinc blende phase below 260 °C with 10% Mn doping could be attributed to the competition between cation ions resulting in the formation of strained crystallites. The temperature change from 260 °C to 290 °C provides the activation energy for all the metastable zinc blende to be transformed into the more stable orthorhombic phase.

Fig. 3 shows the effects of different levels of doping (Mn, 0–30 wt.%) on the structural properties of the obtained SnS nanocrystals. When the doping concentration of Mn was 10 wt. % and the final reaction temperature was 260 °C, a mixed phase of zinc blende and orthorhombic was obtained. At intermediate doping levels (20% Mn), sharp peaks corresponding to both zinc blende and orthorhombic phases are present, resulting in a mixed phase SnS crystal structure similar to the one obtained at 10 wt.% Mn doping, but with the zinc blende peaks having higher intensities. However, at 30 wt.% Mn doping most of the orthorhombic peaks disappear, except the (111) and (040) diffraction planes, which become a broadened peak, while the (111) and (200) planes of the zinc blende phase show sharp intense peaks, resulting in SnS nanocrystals that are predominantly zinc blende (Fig. 3a). The peaks appear to shift to higher angles as the doping concentration is increased to 30 wt.% Mn, resulting in reduced lattice spacing of the planes of the zinc blende phase (Fig. 3b). The size of these near spherical zinc blende nanoparticles is found by Scherrer's equation to be about 20 nm. This clearly shows agglomeration of the zinc blende single crystallites to form larger poly-crystallites, as illustrated in the TEM image (Fig. 3f). The HRTEM image (Fig. 3g) of these crystallites at 30 wt.% Mn doping shows clear lattice planes that demonstrate the crystallinity of the obtained samples. The typical lattice spacings were measured to be 0.35 and 0.28 nm, which corresponds to the distance between the (111) and (200) facets of the zinc blende phase of SnS with a crystal constant, $a = 0.5845$ nm. Burton and Walsh [14] suggested that the formation of the metastable phase could be favored either by rapid growth in high energy environments, or a high concentration of crystal defects. As the competition between Sn and Mn ions increases with an increased doping concentration of Mn, violent reactions occur which only calm down once nucleation is completed, and this results in the formation of crystal defects and favors the formation of the zinc blende phase.

Optical measurements of Mn doped SnS (0% and 30%) thin films show absorption onset for the orthorhombic phase (Mn-0 wt.%) at about 980 nm and the zinc blende phase (Mn-30 wt.%) at about 840 nm. The dependence of the absorption coefficient (α) on the incident photon energy for semiconductors can be written as $(\alpha h\nu)^n = B(h\nu - E_g)$, where n is a number that depends on the electronic transition of the semiconductor and B is a constant. The dependence of α^2 on the photon energy ($h\nu$) for the direct band gap and $\alpha^{0.5}$ on the photon energy for the indirect band gap is illustrated graphically (Fig. 4b and c). Estimates for the direct and indirect band gaps of the orthorhombic SnS phase from the intercepts of the plot are 1.24 and 1.17 eV, respectively. On the other hand, the direct and indirect band gaps of the zinc blende SnS phase from the intercepts of the plot are estimated to be 1.61 and 1.28 eV respectively. The large blue shift in the direct band gap of the zinc blende (Mn-30%) as compared to orthorhombic (Mn-0%) phase SnS cannot be explained by quantum confinement effects, but rather is due to the phase difference in their crystal structures. This occurs because the band structure of a semiconductor, and thus its optical properties, depend strongly on the types of orbital interactions in

the solid and the symmetry (zinc blende or orthorhombic) of their overlap.

The XPS measurements obtained by Electron Spectroscopy for Chemical Analysis (ESCA) reveal the presence of two valence states for tin ions (Sn^{4+} at 486.6 eV and Sn^{2+} at 485.1 eV) and one valence state for sulfur (S^{2-} at 161.8 eV) before and after doping with manganese (Fig. 5a–c). The strong presence of the Sn^{4+} valence state highlights the native p type conduction observed in SnS, due to the small enthalpy during the formation of tin vacancies, which generate shallow acceptors [14]. It can be observed from the XPS spectra that after doping 30 wt.% Mn, the intensity of Sn^{4+} is unchanged, while that of Sn^{2+} drops, indicating that Mn^{2+} replaces Sn^{2+} during the thermal decomposition synthesis. Peaks at 641 eV and 653.5 eV in the XPS spectra correspond to the binding energies of Mn^{2+} and are observed after doping, while they are absent without doping (Fig. 5d). The zinc blende peak shift to higher angles observed in the PXRD results (Fig. 3b) suggests transition to a smaller crystal lattice spacing and also implies that there is a higher probability that the Mn^{2+} substitutes the Sn^{2+} based on their atomic radii (the atomic radii of Sn^{4+} , Sn^{2+} and Mn^{2+} is 0.69, 0.93 and 0.8 Å respectively). Furthermore, PXRD results at different doping concentrations show peaks corresponding to either the orthorhombic or zinc blende phases of SnS, and no peaks corresponding to Mn or any Mn related compounds, which further implies substitutional doping of Mn in SnS. To further clarify this, Extended X-ray Absorption Fine Structure (EXAFS) measurements

need to be performed, as these are sensitive to the local atomic environment of the dopant atoms.

Water splitting under sunlight has received much attention for production of renewable hydrogen from water on a large scale [10,26–29]. Pure and doped SnS nanocrystals were used to prepare thin films coated on conductive FTO/glass substrates and used as a working electrode in a three-electrode photo-electrochemical cell. Fig. 6 shows the photocurrent density of the SnS samples doped with 0, 20 and 30 wt.% Mn. The highest photocurrent density (56.26 $\mu\text{A}/\text{cm}^2$) at an applied potential of 1 V (versus Ag/AgCl) was observed for the 20 wt.% Mn doped SnS nanocrystals (Fig. 6b) which have a metastable and distorted crystal structure owing to the presence of both orthorhombic and zinc blende phases. The different absorption onsets of the two phases result in a wider absorption range and hence higher current densities are observed. The photocurrent density is relatively lower for purely orthorhombic (0–10 wt.% Mn) or zinc blende (30 wt.% Mn) phase SnS and does not improve significantly when compared to the current density in the dark. SnS in its native form often suffers from low incident photon to current efficiency (IPCE) which is thought to be due to charge carrier recombination at the grain boundaries and the presence of sulfur vacancies. The crystal structure and hence the optoelectronic properties of SnS can be tuned by utilizing controlled substitutional doping of metal ions like Mn that could enhance IPCE by introducing localized bands that facilitate improved charge transfer [30].

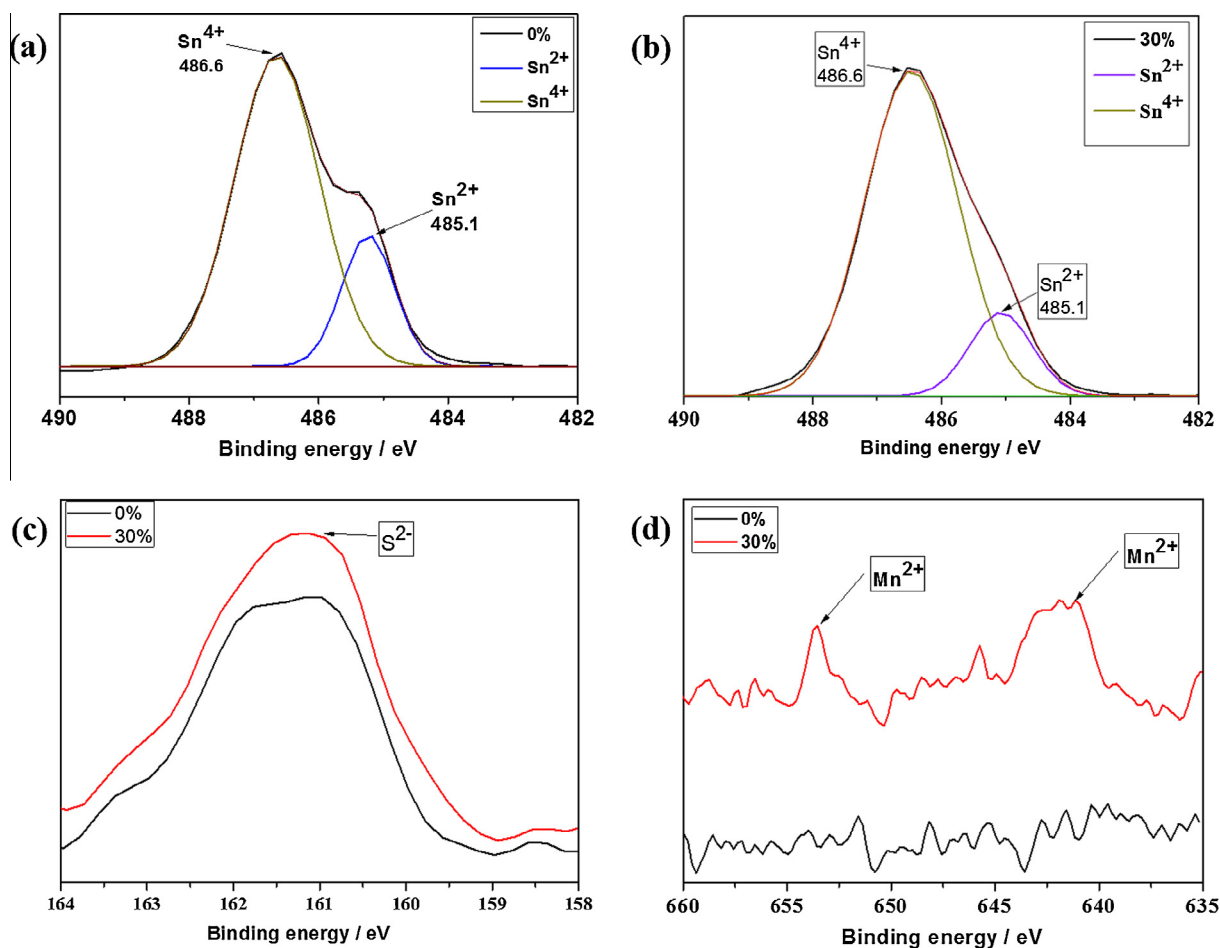


Fig. 5. XPS spectra displays Sn 3d₅ peaks at 486.6 eV and 485.1 eV corresponding to valence states of Sn^{4+} and Sn^{2+} , respectively, in (a) 0% Mn doping and (b) 30% Mn doping. (c) S 2p peak at 161.8 eV which matches the binding energy of S^{2-} ions, and (d) shows Mn 2p₃ peaks at 641 eV and 653.5 eV corresponding to the characteristic binding energies of Mn^{2+} .

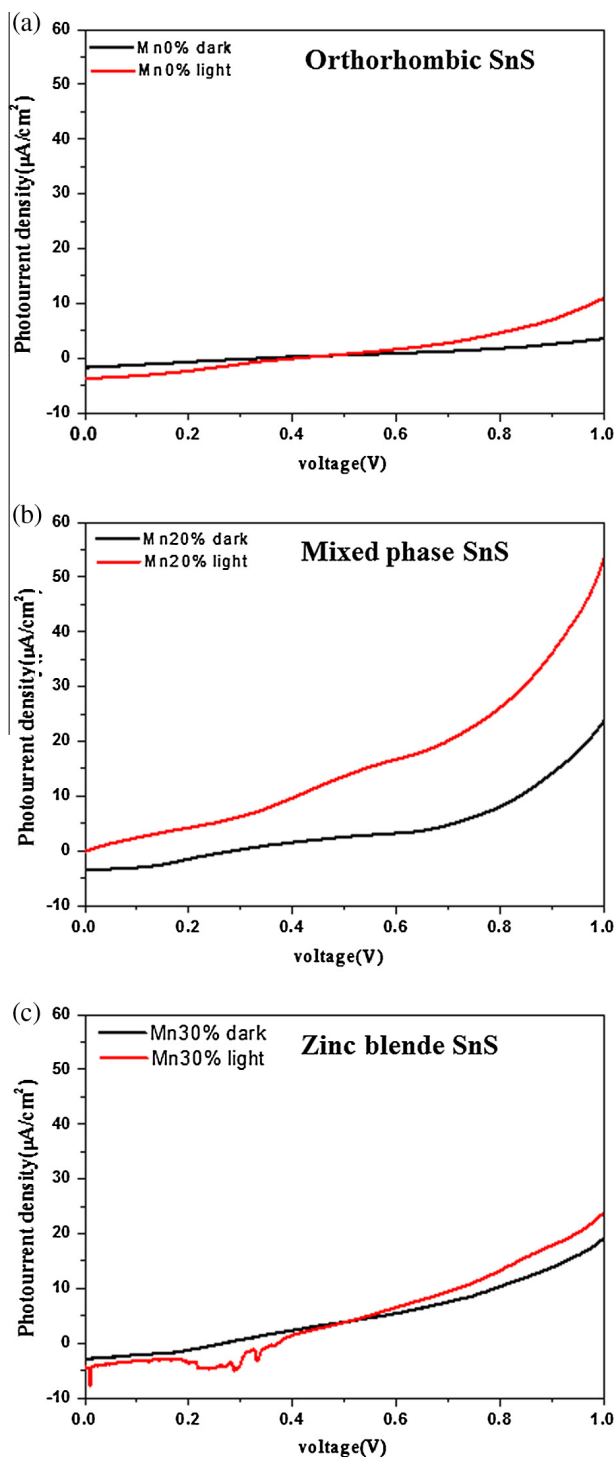


Fig. 6. Photocurrent density as a function of the voltage applied between the working electrode and the counter electrode under irradiation of a 150 W Xe lamp having power density of 50 mW cm^{-2} and in the dark for the (a) pure orthorhombic, (b) mixed phase and (c) pure zinc blende working electrodes.

4. Conclusion

In summary, we have successfully synthesized nanoparticles of the pure zinc blende phase using a thermal decomposition method by the doping of Mn in SnS (30 wt.%). A mixed zinc blende and orthorhombic phase was observed at lower doping concentrations, while pure orthorhombic phase was observed without doping. The

structural and optical properties of the zinc blende phase vary with that of the more stable orthorhombic phase. Higher photocurrent densities were observed for the mixed phase as compared to pure orthorhombic or zinc blende phases. The direct and indirect band gaps for orthorhombic SnS were found to be 1.24 and 1.17 eV, respectively, and for zinc blende phase these were at 1.61 and 1.28 eV, respectively. The shift to absorption of higher energy photons observed in the zinc blende phase can be utilized in future SnS photovoltaic and photo electrochemical cells, and this reinforces the potential of earth abundant IV–VI semiconductor nanostructures.

Acknowledgements

This project was financially supported by the Ministry of Science and Technology of the ROC under contract No. MOST 104-2221-E-218-005-.

References

- [1] J.M. Chamberlain, M. Merdan, Ir photoconductivity in P-sns/P-sns, *J. Phys. C Solid State* 10 (1977) L571–L574.
- [2] M. Devika, K.T.R. Reddy, N.K. Reddy, K. Ramesh, R. Ganesan, E.S.R. Gopal, K.R. Gunasekhar, Microstructure dependent physical properties of evaporated tin sulfide films, *J. Appl. Phys.* 100 (2006).
- [3] A. Tanusevski, Optical and photoelectric properties of SnS thin films prepared by chemical bath deposition, *Semicond. Sci. Technol.* 18 (2003) 501–505.
- [4] D.S. Koktysh, J.R. McBride, R.D. Geil, B.W. Schmidt, B.R. Rogers, S.J. Rosenthal, Facile route to SnS nanocrystals and their characterization, *Mater. Sci. Eng. B-Adv.* 170 (2010) 117–122.
- [5] H.T. Liu, Y. Liu, Z. Wang, P. He, Facile synthesis of monodisperse, size-tunable SnS nanoparticles potentially for solar cell energy conversion, *Nanotechnology* 21 (2010).
- [6] J. Liu, D.F. Xue, Sn-based nanomaterials converted from SnS nanobelts: facile synthesis, characterizations, optical properties and energy storage performances, *Electrochim. Acta* 56 (2010) 243–250.
- [7] Z.T. Deng, D.R. Han, Y. Liu, Colloidal synthesis of metastable zinc-blende IV–VI SnS nanocrystals with tunable sizes, *Nanoscale* 3 (2011) 4346–4351.
- [8] P.S. Tang, H.F. Chen, F. Cao, G.X. Pan, K.Y. Wang, M.H. Xu, Y.H. Tong, Nanoparticulate SnS as an efficient photocatalyst under visible-light irradiation, *Mater. Lett.* 65 (2011) 450–452.
- [9] D. Avellaneda, M.T.S. Nair, P.K. Nair, Photovoltaic structures using chemically deposited tin sulfide thin films, *Thin Solid Films* 517 (2009) 2500–2502.
- [10] Y.F. Sun, H. Cheng, S. Gao, Z.H. Sun, Q.H. Liu, Q. Liu, F.C. Lei, T. Yao, J.F. He, S.Q. Wei, Y. Xie, Freestanding tin disulfide single-layers realizing efficient visible-light water splitting, *Angew. Chem. Int. Ed.* 51 (2012) 8727–8731.
- [11] N.K. Reddy, K.T.R. Reddy, Growth of polycrystalline SnS films by spray pyrolysis, *Thin Solid Films* 325 (1998) 4–6.
- [12] E.C. Greyson, J.E. Barton, T.W. Odom, Tetrahedral zinc blende tin sulfide nanoand microcrystals, *Small* 2 (2006) 368–371.
- [13] D. Avellaneda, M.T.S. Nair, P.K. Nair, Polymorphic tin sulfide thin films of zinc blende and orthorhombic structures by chemical deposition, *J. Electrochem. Soc.* 155 (2008) D517–D525.
- [14] L.A. Burton, A. Walsh, Phase stability of the earth-abundant tin sulfides SnS, SnS₂, and Sn₂S₃, *J. Phys. Chem. C* 116 (2012) 24262–24267.
- [15] Z.T. Deng, D. Cao, J. He, S. Lin, S.M. Lindsay, Y. Liu, Solution synthesis of ultrathin single-crystalline SnS nanoribbons for photodetectors via phase transition and surface processing, *ACS Nano* 6 (2012) 6197–6207.
- [16] H. Tang, J.G. Yu, X.F. Zhao, D.H.L. Ng, Influence of PSSS on the morphology and polymorph of calcium carbonate in the ethanol-water mixed system, *J. Alloys Compd.* 463 (2008) 343–349.
- [17] S.Y. Hong, R. Popovitz-Biro, Y. Prior, R. Tenne, Synthesis of SnS₂/SnS fullerene-like nanoparticles: a superlattice with polyhedral shape, *J. Am. Chem. Soc.* 125 (2003) 10470–10474.
- [18] Q. Li, Y. Ding, H. Wu, X.M. Liu, Y.T. Qian, Fabrication of layered nanocrystallites SnS and beta-SnS₂ via a mild solution route, *Mater. Res. Bull.* 37 (2002) 925–932.
- [19] G.Z. Shen, D. Chen, K.B. Tang, L.Y. Huang, Y.T. Qian, G. Zhou, Novel polyol route to nanoscale tin sulfides flaky crystallines, *Inorg. Chem. Commun.* 6 (2003) 178–180.
- [20] H.L. Su, Y. Xie, Y.J. Xiong, P. Gao, Y.T. Qian, Preparation and morphology control of rod-like nanocrystalline tin sulfides via a simple ethanol thermal route, *J. Solid State Chem.* 161 (2001) 190–196.
- [21] C.H. An, K.B. Tang, Y. Jin, Q.C. Liu, X.Y. Chen, Y.T. Qian, Shape-selected synthesis of nanocrystalline SnS in different alkaline media, *J. Cryst. Growth* 252 (2003) 581–586.
- [22] C.H. An, K.B. Tang, G.Z. Shen, C.R. Wang, Q. Yang, B. Hai, Y.T. Qian, Growth of belt-like SnS crystals from ethylenediamine solution, *J. Cryst. Growth* 244 (2002) 333–338.

- [23] T. Hyeon, S.S. Lee, J. Park, Y. Chung, H. Bin Na, Synthesis of highly crystalline and monodisperse maghemite nanocrystallites without a size-selection process, *J. Am. Chem. Soc.* 123 (2001) 12798–12801.
- [24] P. Sinsersuksakul, R. Chakraborty, S.B. Kim, S.M. Heald, T. Buonassisi, R.G. Gordon, Antimony-doped tin(II) sulfide thin films, *Chem. Mater.* 24 (2012) 4556–4562.
- [25] B.K. Patra, S. Sarkar, A.K. Guria, N. Pradhan, Monodisperse SnS nanocrystals: in just 5 seconds, *J. Phys. Chem. Lett.* 4 (2013) 3929–3934.
- [26] A. Kudo, Y. Miseki, Heterogeneous photocatalyst materials for water splitting, *Chem. Soc. Rev.* 38 (2009) 253–278.
- [27] X.B. Chen, S.H. Shen, L.J. Guo, S.S. Mao, Semiconductor-based photocatalytic hydrogen generation, *Chem. Rev.* 110 (2010) 6503–6570.
- [28] K. Maeda, K. Domen, Photocatalytic water splitting: recent progress and future challenges, *J. Phys. Chem. Lett.* 1 (2010) 2655–2661.
- [29] M.G. Walter, E.L. Warren, J.R. McKone, S.W. Boettcher, Q.X. Mi, E.A. Santori, N.S. Lewis, Solar water splitting cells, *Chem. Rev.* 110 (2010) 6446–6473.
- [30] B. Subramanian, C. Sanjeeviraja, M. Jayachandran, Review on materials properties of Sn(S, Se) compound semiconductors useful for photoelectrochemical solar cells, *B Electrochem.* 18 (2002) 349–366.